Int. J. Electrochem. Sci., 17 **(2022)** Article Number: 221184, doi: 10.20964/2022.11.86

International Journal of
ELECTROCHEMICAL
SCIENCE
www.electrochemsci.org

Investigation on Erosion-Corrosion Behavior of Q235 Steel in Liquid-Solid Flow Using Electrochemical Method and Numerical Simulation

Feng Wang, Wei Xu, Hui Huang[*]*, Chang-chun Li, Li-qiu Chen*

China Special Equipment Inspection & Research Institute, Beijing, 100029, China
[*]E-mail: huanghui@126.com

Received: 7 September 2022 / *Accepted:* 2 October 2022 / *Published:* 20 October 2022

With the rapid increase of sand content in crude oil, erosion corrosion has gradually become the key factor of pipeline failure, especially for the elbow. Therefore, in this paper, the corrosion rate, corrosion morphology, electrochemical experiment and numerical simulation were investigated to study the erosion-corrosion behavior of 90° elbow. The results showed that with the increase of experiment time, the corrosion rate of Q235 steel at different angles showed increased linearly, while the max pitting depth basically remained unchanged. In the inlet section of θ=0-45°, Q235 steel was subjected to the joint action of erosion and impact. With the increase of angle, the breakage degree of corrosion product layer on Q235 steel surface became more serious. In the outlet section of θ=45°-90°, Q235 steel was only affected by erosion, and the distribution of corrosion products and holes had obvious directionality. The pure erosion process can be divided into three stages of the formation of erosion morphology, development in the longitudinal direction and general erosion. Under the conditions studied in this paper, the current density of pure erosion was only 42.16% of that of erosion-corrosion. The reason was mainly that the loose FeO(OH) can promote the electrochemical process and also accelerate the diffusion of products.

Keywords: Erosion-corrosion behavior; Q235 steel; Liquid-solid flow; Electrochemical method; Numerical simulation

1. INTRODUCTION

Erosion-corrosion is one of the main causes of pipeline corrosion and perforation in petroleum-petrochemical field. Because the erosion damage is affected by many factors such as material properties, fluid mechanics conditions and the environment, the research process of erosion-corrosion is complicated [1-3]. Among these, the liquid-solid two-phase flow erosion-corrosion is representative of the multiphase-flow erosion-corrosion [1-4]. Erosion and corrosion is a relation of mutual influence,

in which the study on erosion-corrosion of the pipe wall should not only consider the mechanics under the repeated impact, but also focus on the electrochemical reaction process. Therefore, the material total loss caused by erosion-corrosion is often greater than the sum of that caused by pure erosion and pure corrosion [5-9].

In detail, the interaction of erosion-corrosion included the influence of erosion on corrosion and the influence of corrosion on erosion [10]. Generally speaking, the interaction of on corrosion was mainly that through high-speed erosion, the surface mass transfer process was accelerated to promote depolarization agent reaching the material surface, and then the stripping of corrosion products was accelerated [11-13]. Moreover, particle impact will destroy or rapidly thin the passive film on the surface of the material, resulting in the exposure of the new active metal surface, and then increase the electrochemical corrosion reaction area, thus accelerating the corrosion rate. From the other aspect, through chemical reaction or electrochemical reaction, the surface of the material became loose and porous, promoting the diffusion of the protected corrosion product [14,15]. The interaction between the two processes was synergy, which can be expressed as positive synergy and negative synergy for different research systems. Compared with negative synergistic effect, most research results showed positive synergistic effect, that is, further increased the degree of erosion-corrosion damage [16].

Focusing on the synergistic effect, Islam et al. [17] designed a test device to obtain the total loss rate of API X70 steel as well as the components of erosion, corrosion and their synergistic effects. The results showed that scour and corrosion promoted each other and produced a positive synergistic effect [18-21]. Joshua et al. [22] conducted immersion experiment at a flow rate of 20 m/s in 2 wt.% NaCl containing particles with an average diameter of 250 μm in 1000 mg/L at 60℃ in pH=4.7, and found that the erosion-corrosion rate promoted by the corrosion a accounted for 20% of total erosion-corrosion rate. The microstructure morphology showed that corrosion promoted the fatigue crack propagation and accelerated the material damage. Raheem et al. [23] studied the interaction between erosion and corrosion of 90° elbow of 1018 steel. The results showed that the erosion effect of particles can be improved by increasing the velocity and concentration, thus the erosion-corrosion rate of the elbow can be increased. The synergistic effect was 56% at 2.5 m/s, while the synergistic effect decreased to 11% at 4 m/s [24]. Zhou et al. [25] used a rotating cylindrical electrode system for electrochemical measurement to study the synergistic effect of erosion and corrosion on low carbon steel in carbonate-bicarbonate solution. The results showed that erosion significantly increased the corrosion rate, and the influence mechanism of corrosion on erosion changed with the application of potential. In addition, Tan et al. [26] used conventional weight loss measurement and electrochemical noise technology to identify and quantify the synergistic effect, and their study proved for the first time that there was a correlation between the standard deviation ratio of electrochemical current noise and erosion weight loss data. Therefore, in this paper, based on the combination of experimental and simulated method, the corrosion rate, corrosion morphology, electrochemical test and numerical simulation were investigated to study the erosion-corrosion behavior of 90° elbow.

2. EXPERIMENTAL SETTINGS

2.1 Erosion-corrosion experiment

An erosion-corrosion test device was designed, including water tank, centrifugal pump, frequency converter, flow meter, cooling system, valve, thermometer, pressure gauge, pipe and test elbow, as shown in Figure 1. The device adopted a detachable test elbow, and the inner wall of the test elbow was provided with a plurality of grooves for placing test samples, so as to realize the weight loss measurement of erosion-corrosion of the test elbow. The experimental device can be used to simulate the actual working conditions of pipelines, study the change law of erosion-corrosion characteristics of different parts of elbow with time, and reveal the mechanism of scour corrosion failure of elbow.

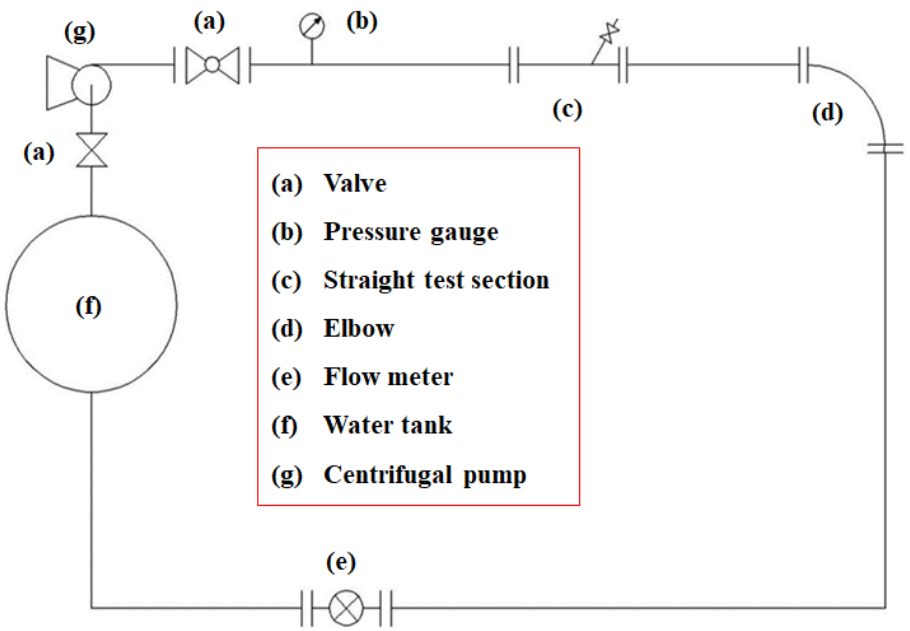

Figure 1. Erosion-corrosion test device

In this paper, 7 test pieces were encapsulated at different angles outside the elbow, as shown in Figure 2. The material of the test pieces was Q235 steel with the size of 7×7×2 mm^3, the main components were shown in Table 1. The inner diameter of the elbow was 0.051 m, and the flow rate was set at 3 m/s. The solid was quartz sand with a particle size of 100-110 mesh and a sand content of 2% [27]. The experimental solution was 3 wt.% NaCl solution prepared by analytically pure NaCl and deionized water, and the experimental temperature was 20℃.

The erosion-corrosion experiment under different experiment time was carried out, and 5 groups of parallel experiments were set. The experiment period was 30 h. A group of test pieces were taken out every 6 h, and the erosion-corrosion morphology of Q235 steel surface was observed by SEM. The weight loss test was carried out after removing the corrosion products on the surface. The maximum pit depth of Q235 steel was measured by 3D microscope.

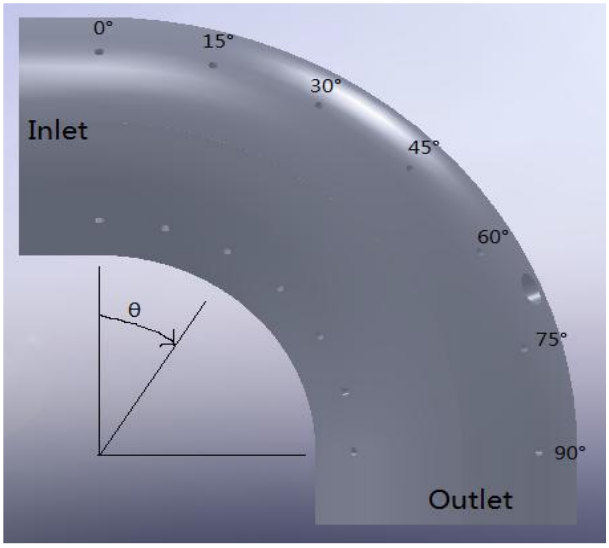

Figure 2. Position distribution of the Q235 samples of the experimental elbow

Table 1. The main component of Q235 steel (mass fraction, wt. %)

C	Mn	Si	S	P	Fe
0.20	1.4	0.35	0.045	0.045	Ceq

The cathodic protection with the potential of -1.0 V (vs. saturated calomel electrode) was applied to Q235 steel samples at different positions to simulate pure erosion environment [28]. The changes of current density with time of Q235 steel samples at different locations in pure erosion and erosion-corrosion environments were tested, and the corrosion products were analyzed to reveal the mechanical-electrochemical effect of erosion-corrosion.

2.2 Numerical simulation of erosion-corrosion on 90° elbow

In this paper, the Fluent software was used to simulate and calculate the hydrodynamics parameters of erosion-corrosion of elbow at a flow rate of 3 m/s with the sand content of 2%.

Considering the stable flow state of the fluid in the elbow to facilitate full diffusion of sand in the fluid, a straight pipe section in the length of 1 m was added to the inlet section of the elbow, and a straight pipe section in the length of 1 m was added to the outlet section of the elbow. The inner diameter (D) of the elbow was 0.051 m, and the radius (R) of curvature was 0.0765 m (i.e. 1.5 D) [29]. Gambit software was used to carry out structural mesh division of the geometric model, in which the mesh interval was 0.0032 m and the total number of meshes was 371582, ensuring the quality of meshes to meet the requirements. DPM (discrete phase) model was used to simulate the erosion model of liquid-solid two-phase flow in the elbow, and the particle trajectory was simulated [30]. The liquid phase was 3 wt.% NaCl solution, and the solid phase was sand. The inlet condition was velocity inlet, and the outlet was free outflow. The k-ε turbulence model was selected, and the convergence criterion was 0.000001.

3. RESULTS AND DISCUSSION

3.1 Corrosion rate

Figure 3 showed the variation of corrosion rate (i.e. erosion-corrosion rate) and max pitting depth of Q235 steel at different angles with time. As can be seen from the Figure 4(a), the corrosion rate of Q235 steel at different angles increased linearly with the increase of experiment time [31], as shown in Table 2.

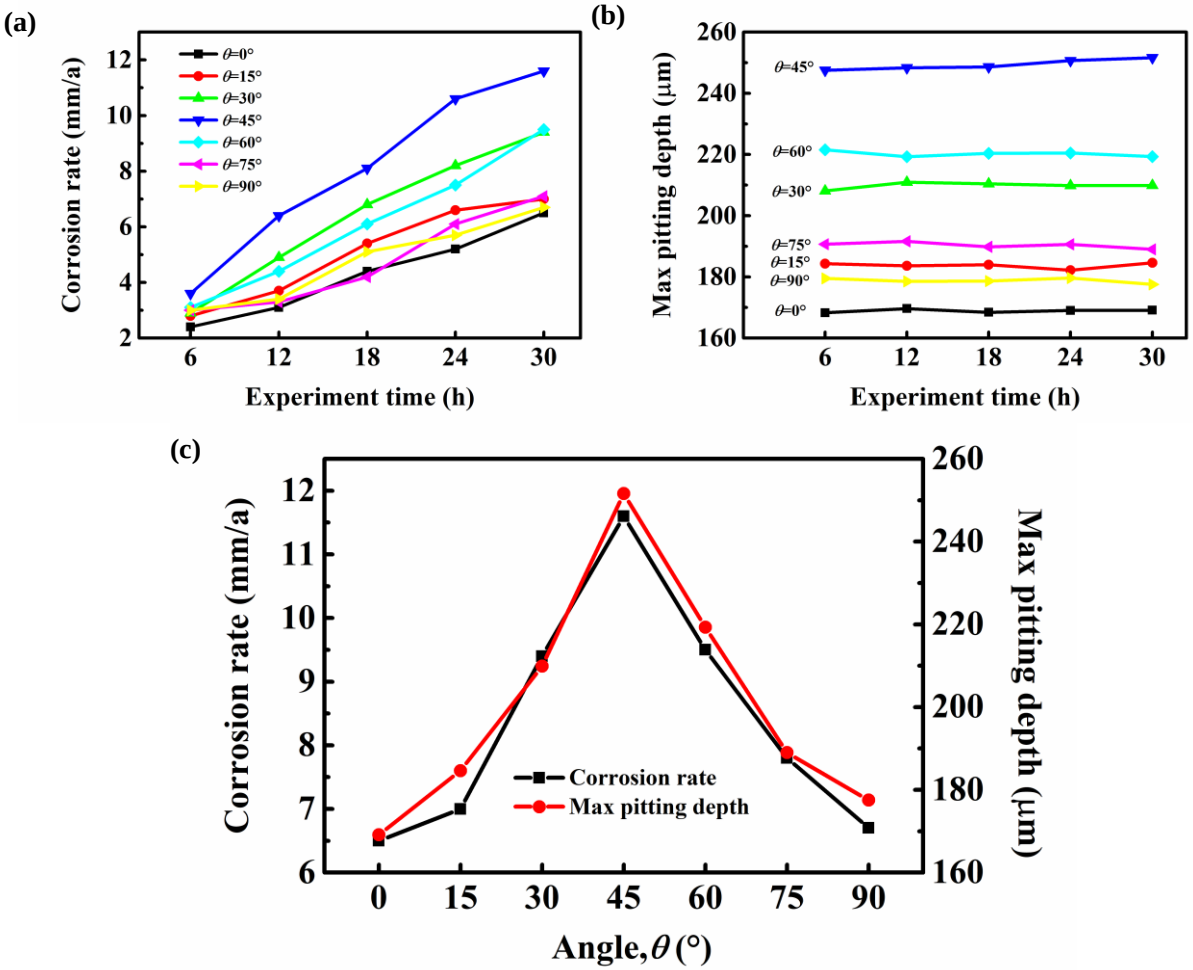

Figure 3. The variation of corrosion rate and max pitting depth of Q235 steel at different angles with time: (a) Corrosion rate (i.e. Erosion-corrosion rate), (b) Max pitting depth, and (c) Corrosion rate and Max pitting depth at 30 h

It can be seen from the Figure 4(c) that with the increase of angle (θ), the increase rate of corrosion rate and corrosion rate all firstly increased and then decreased, reaching the maximum at θ=45°. Generally speaking, the increase rate in θ=45-90° was slightly smaller than that in θ=0-45°, namely, 0.1617 (θ=90°) < 0.1717 (θ=0°), 0.1833 (θ=75°) < 0.1883 (θ=15°), and 0.2650 (θ=60°) < 0.2717 (θ=30°) [32-35]. On the contrary, the corrosion rate at 30 h in θ=45-90° was slightly greater than that in θ=0-45°, namely, 6.77 (θ=90°) > 6.51 (θ=0°), 7.15 (θ=75°) > 7.03 (θ=15°), and 9.58

(θ=60°) > 9.44 (θ=30°) [36,37]. However, with the increase of the experiment time, the maximum pitting depth of Q235 steel at different angles basically remains unchanged, as shown in Figure 4(b). Taking the max pitting depth at 30 h as an example, it can be seen from Figure 4(c) that the max pitting depth firstly increased and then decreased with the angle, and also reached the maximum (251.634 μm) at θ=45° [38]. And similarly, the max pitting depth at 30 h in θ=45°-90° was slightly greater than that in θ=0-45°, namely, 177.524 (θ=90°) > 169.112 (θ=0°), 188.991 (θ=75°) > 184.637 (θ=15°), and 219.319 (θ=60°) > 209.889 (θ=30°) [39]. Therefore, based on the results of corrosion rate and max pitting depth, it can be seen that the corrosion degree of pipe in θ=45°-90° was comprehensively in θ=45°-90° greater than that in θ=0-45°.

Table 2. Fitting equations of corrosion rate (y) and experiment time (x) of Q235 steel at different angles

Angle	Fitting equation	R^2
θ=0°	y=0.1717·x+1.23	0.9908
θ=15°	y=0.1883·x+1.23	0.9673
θ=30°	y=0.2717·x+1.23	0.9880
θ=45°	y=0.3367·x+1.23	0.9801
θ=60°	y=0.2650·x+1.35	0.9969
θ=75°	y=0.1833·x+1.44	0.9444
θ=90°	y=0.1617·x+1.23	0.9692

3.2 Corrosion morphology

Figure 4 showed the variation of microscopic morphology of Q235 steel at different angles with time.

As can be seen from the figure, at the initial experiment stage of 6 h, the corrosion product layer on the surface of Q235 steel was relatively intact at different positions, and there were obvious cracks and fractures at θ=45° compared with other positions. With the increase of experiment time, under the condition in this paper, the Q235 steel at θ=0° and θ=90° was less affected by the erosion, due to that these two positions can be considered horizontal with the direction of liquid-solid two-phase flow [40]. However, the roughness of corrosion product layer of Q235 steel at θ=0° was much larger than that at θ=90°, while there were obvious pits on the surface of Q235 steel at θ=90°, which was mainly caused by the difference of solid particles' sharpness [41].

In the inlet section of θ=0-45°, Q235 steel is subjected to a combination of erosion and impact, in which the greater the angle was, the greater the impact force of the vertical effect on Q235 steel was, the more serious breakage of corrosion product layer was. For example, corrosion product layer of Q235 steel at θ=30° was dispersed [42-45]. In addition, the impact momentum component of solid particles was equal to the erosion momentum component. The corrosion product layer on Q235 steel surface was densely covered with small holes and obvious directivity. In the outlet section of θ=45°-90°, Q235 steel was only affected by erosion. From the corrosion morphology, it can be seen that the distribution of corrosion products and holes showed obvious directivity, and the larger the angle was,

the less obvious the directivity was, indicating that the erosion effect was less [46]. For another aspect, the erosion effect on the outlet section was greater than that on the inlet section [47], so the corrosion rate and the max pitting depth in Figure 4 were larger.

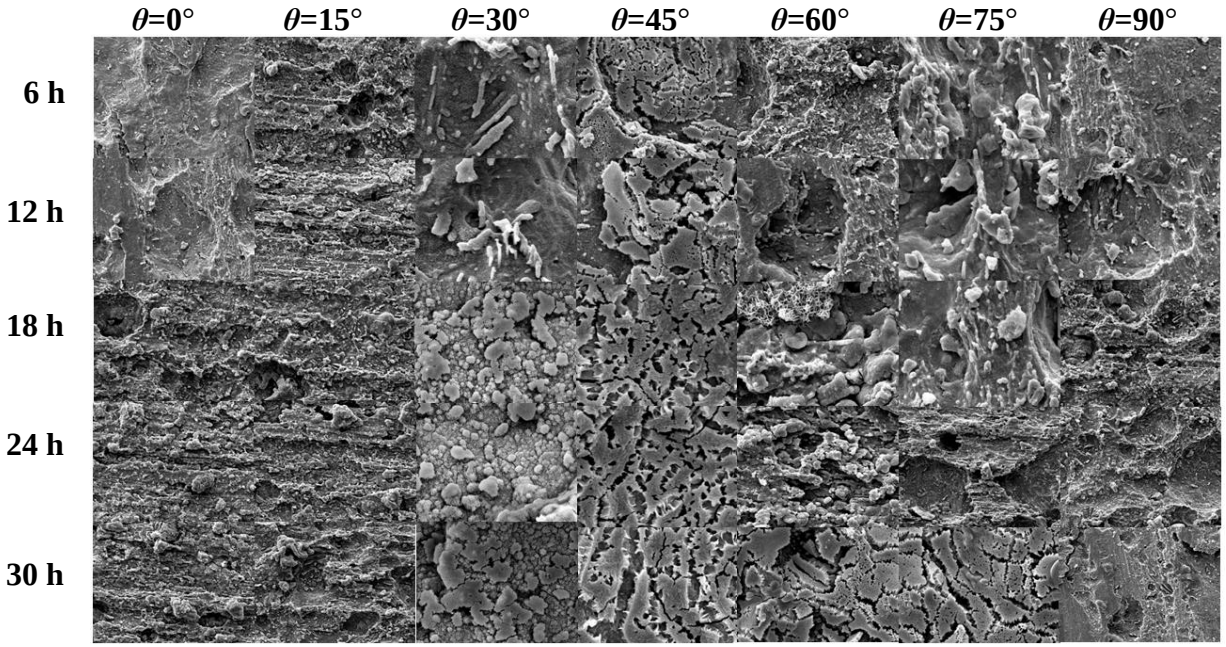

Figure 4. The variation of microscopic morphology of Q235 steel at different angles with time

3.3 Electrochemical test

Figure 5 showed the variation of current density of Q235 steel at different angles with time under pure erosion and erosion-corrosion conditions. As can be seen from the figure, under pure scouring condition, the current density fluctuated between 0.296-0.430 μA/m^2, which can be divided into three stages [48]. At 0-24 h, with the increase of pure erosion time, the current density of Q235 steel at different angles increased, which was mainly because the erosion morphology was forming at this time, indicating that the surface roughness of Q235 steel increased, and the metal weight loss rate became faster [49-52]. At 24-48 h, at this time, the surface erosion morphology of Q235 steel had been formed, and the erosion morphology developed in the longitudinal direction. The development of local characteristics led to the reduction of the general current density of Q235 steel. When the erosion lasted for 48-72 h, the current density increased, which was caused by the transition from local erosion to general erosion [53]. In addition, the larger the angle was, that is, the closer to the exit position, the greater the variation of current density was. It was worth noting that, in the process of pure erosion, the current density generally presented a similar sinusoidal variation law with the change of time. Taking the average value of I_c = 0.36 μA/m^2 as the base, the maximum was 0.43 μA/m^2 at 24 h, and the minimum value was 0.29 μA/m^2 at 48 h, indicating that the current density was realized to be approximately symmetric distribution.

Under the erosion-corrosion condition, the current density of Q235 steel at different angles

increased with experiment time, showing the mutual promotion of electrochemical general corrosion and locally erosion. However, at the initial time of 6 h, the current density of Q235 steel at different angles was less than that of pure erosion. When the erosion-corrosion time reached 72 h, taking Q235 steel at θ=45° as an example, the current density of pure erosion was only 0.430 μA/m^2, while the current density of erosion-corrosion was 1.020 μA/m^2, indicating that mechanical-electrochemical processes promoted each other, and the pure erosion process only took up 42.16% [54]. Moreover, in the erosion-corrosion process, the erosion-corrosion current density at different positions was located between that of θ=45° and θ=90°. By fitting two curves of current density with time, the slopes were 0.0157 at θ=45° and 0.076 at θ=90°, respectively. It can be approximated that pure erosion accounted for 0.076/0.0157=48.41% of erosion-corrosion, which was basically consistent with the above example of 42.16%.

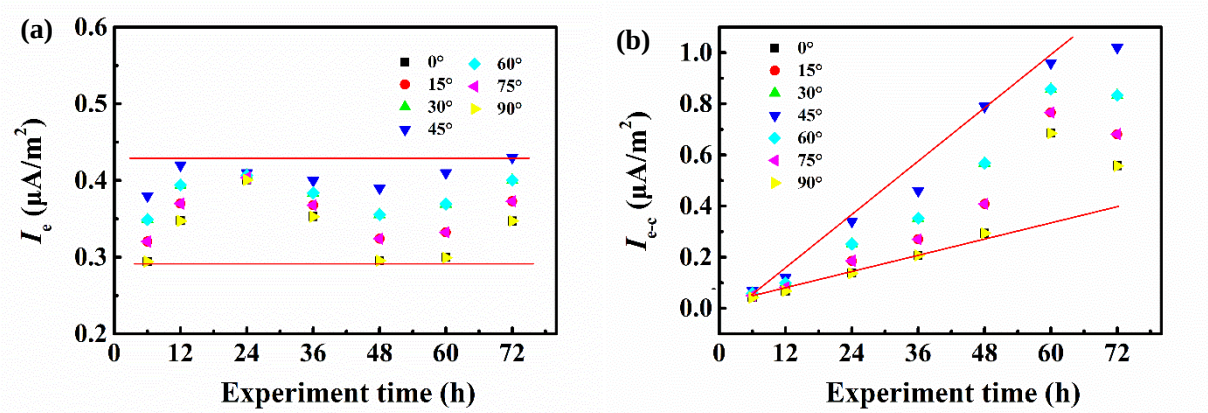

Figure 5. The variation of current density of Q235 steel at different angles with time: (a) I_e was the current density of pure erosion, and (b) I_{e-c} was the current density of erosion-corrosion

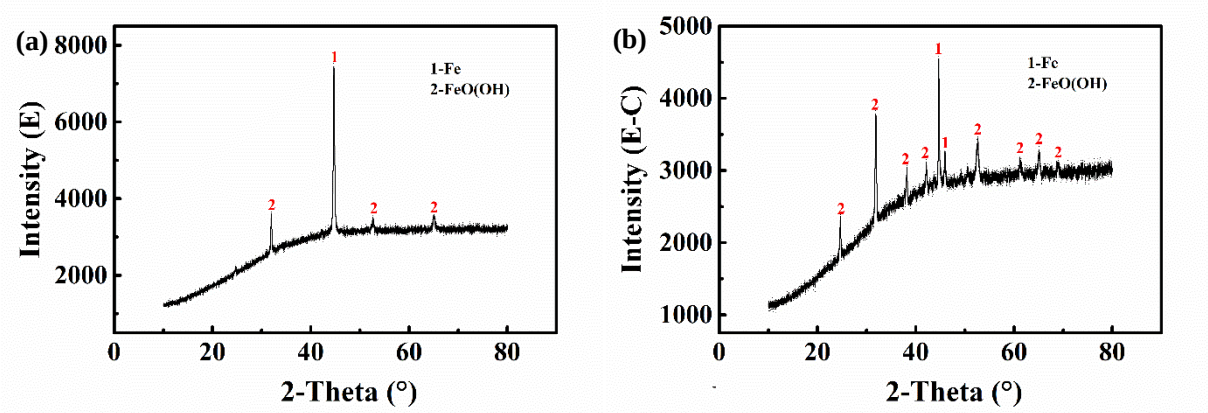

Figure 6. The corrosion products of Q235 steel at θ=45° and t = 72 h: (a) pure erosion, and (b) erosion-corrosion

Taking Q235 steel at t = 72 h and θ=45° as an example, the main components of products on the surface under pure erosion and erosion-corrosion conditions were analyzed, as shown in Figure 7. It can be seen that under pure erosion condition, the product was consisted of Fe and few FeO(OH)

[55]. Under the erosion-corrosion condition, the content of FeO(OH) increased significantly. FeO(OH) with the loose and porous characteristic [55,56] can promote the diffusion of corrosive medium to the surface of Q235 steel and then promote the electrochemical corrosion process of Q235 steel, thus aggravating the erosion-corrosion effect.

3.4 Numerical simulation

In order to reveal the erosion-corrosion mechanism of 90° elbow, the flow characteristics and erosion characteristics of the elbow under the liquid-solid two-phase flow condition with sand content of 2% and flow rate of 3 m/s were calculated by CFD numerical simulation. Figure 10 was the results of numerical simulation. It can be seen that there were great differences in the flow characteristics of liquid-solid two-phase flow at different parts of the elbow, as well as in the distribution of sand concentration.

Figure 7(a) was the velocity nephogram at different angles. Due to the curved geometry structure of the elbow, the mixed fluid in the elbow was forced to change its flow direction by centrifugal force, and the fluid in the center of the elbow was thrown near the outer wall of the elbow, resulting in greater fluid pressure near the outer wall and smaller fluid pressure near the inner wall. Therefore, in the inlet section of the elbow, the max velocity at different angles tended to the outside, and the distribution of the velocity of each section was basically an eccentric circle [58]. Under this circumstance, due to the influence of elbow geometry and secondary flow, the max velocity in θ=30°-90° gradually deviated to the outside of the elbow, and the velocity distribution of the section at different angles became more complicated [58]. Figure 7(b) was velocity vector nephogram at different angles. At θ=0°, the fluid was less affected by the elbow structure and the velocity distribution was more uniform. The phenomenon of secondary flow appeared from the pipe section at θ=15°, and the secondary flow developed with the increase of angle. The intensity of secondary flow reached the maximum at θ=90°. This was because under the action of centrifugal force, the pressure near the outer wall of the elbow was higher, while the pressure near the inner wall was lower, so the pressure gradient was generated perpendicular to the mainstream direction, resulting in that the central fluid flowed not only along the axis of the pipeline, but also perpendicular to the axis of the elbow. Due to the continuity of fluid flow, the fluid near the outer wall of the elbow was forced to flow near the inner wall, so two vortices will be generated in the elbow, and the rotation direction was opposite, that is, the formation of secondary flow. Figure 7(c) was the sand concentration nephogram at different angles. Due to the influence of gravity, the sand concentration at different angles was obviously stratified. The concentration distribution can be roughly divided into two regions, including the low concentration area in the upper part of the elbow and the high concentration area in the lower part of the elbow. In the inlet section of θ=0-45°, due to the little influence of the elbow geometry structure, the sand stratified in upper and lower sections of the elbow [59], and the symmetrical distribution of sand concentration appeared in inner and outer sections. In θ=30°-90°, with the increase of angle, the distribution of sand concentration became more complex, presenting an asymmetrical distribution in inside and outside sections, in which the high concentration area at the bottom gradually shifted to the outer wall of the elbow [60]. This was because there was a density difference between liquid and solid phase, and the

liquid and solid phase was separated under the action of inertia force and centrifugal force. The sand with high density tended to the outside of the elbow, increasing the concentration of sand near the outer wall.

Figure 8 was the erosion-corrosion nephogram. The pipe section with severe erosion-corrosion occurred in the bottom of the 90° elbow, the outside wall and the outlet section in θ=45°-90°. Especially, the lower part of the elbow was more seriously eroded than the upper part [61,62], which was completely consistent with the area where the erosion rate of the 90° elbow was serious measured in the experiment test.

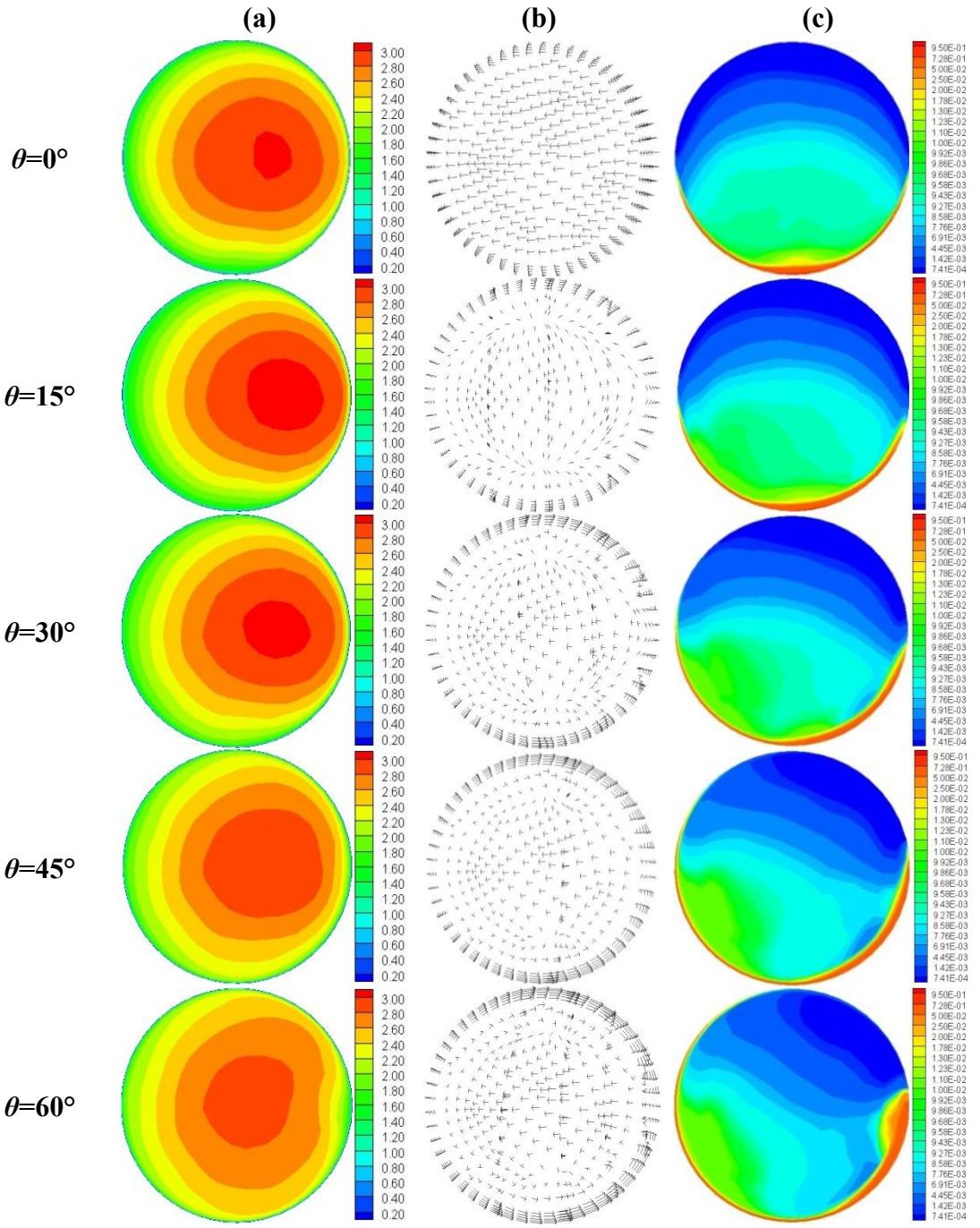

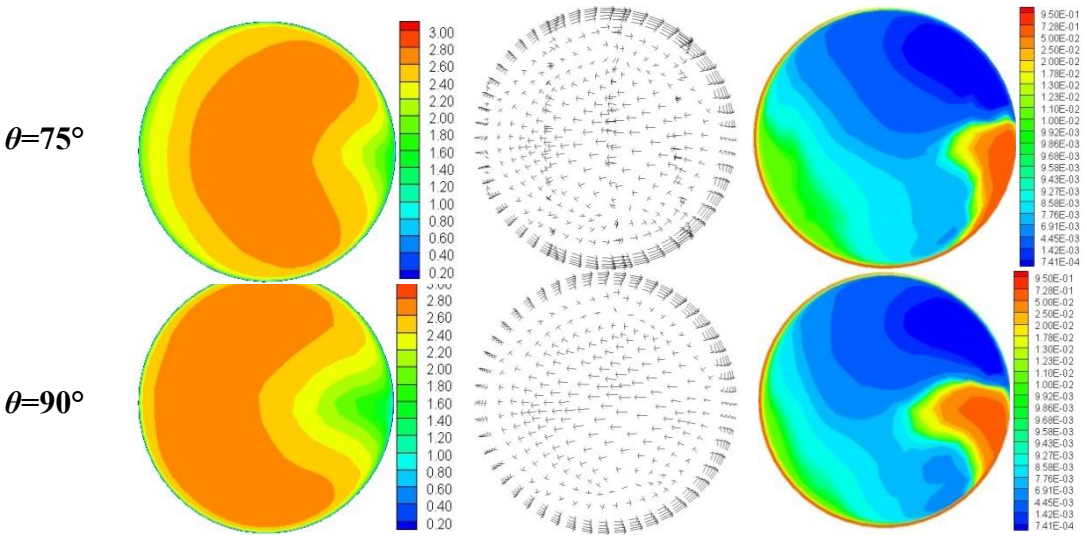

Figure 7. The results of numerical simulation: (a) Velocity nephogram, (b) Velocity vector nephogram, and (c) Sand concentration nephogram

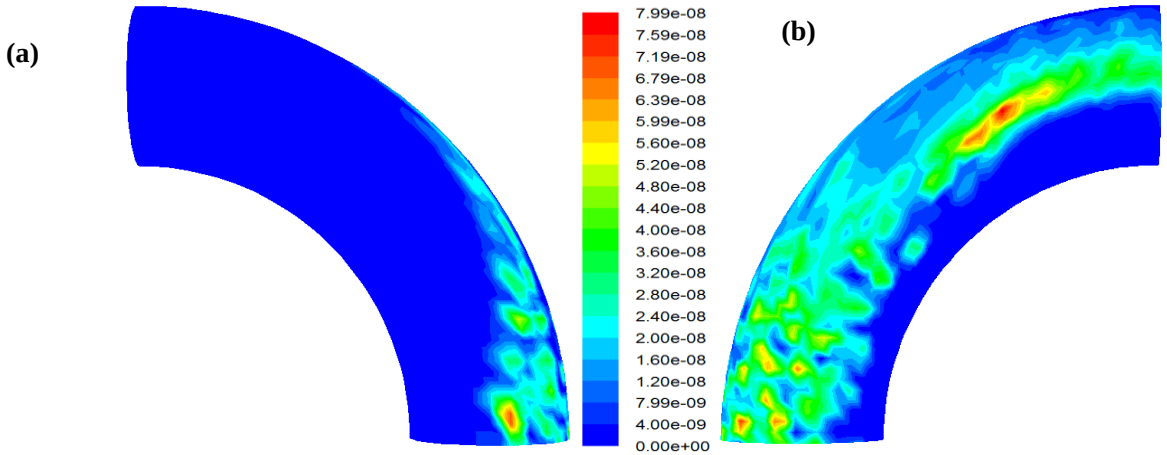

Figure 8. Erosion-corrosion nephogram of 90° elbow: (a) Vertical view, and (b) Bottom view

4. CONCLUSION

In this paper, the corrosion rate, corrosion morphology, electrochemical experiment and numerical simulation were investigated to study the erosion-corrosion behavior of 90° elbow. The following conclusions were drawn.

(1) With the increase of experiment time, the corrosion rate of Q235 steel at different angles showed increased linearly, while the max pitting depth basically remained unchanged. The corrosion rate and the max pitting depth of the outlet section were all greater than those of inlet section at the corresponding angle, reaching the maximum at θ=45°.

(2) In the inlet section of θ=0-45°, Q235 steel was subjected to the joint action of erosion and impact. With the increase of angle, the breakage degree of corrosion product layer on Q235 steel surface became more serious. At θ=0-45°, the corrosion product layer of Q235 steel surface was

densely covered with small holes with obvious directivity. In the outlet section of θ=45°-90°, Q235 steel was only affected by erosion, and the distribution of corrosion products and holes had obvious directionality, and the larger the angle was, the less obvious directionality was.

(3) The pure erosion process can be divided into three stages of the formation of erosion morphology, development in the longitudinal direction and general erosion. Under the conditions studied in this paper, the current density of pure erosion was only 42.16% of that of erosion-corrosion. The reason was mainly that the loose FeO(OH) can promote the electrochemical process and also accelerate the diffusion of products.

(4) The numerical simulation results showed that due to the effect of the elbow geometry structure, secondary flow was formed in the pipe section of θ=30°-90°, and sand concentration was concentrated in the outer and lower part of the elbow, resulting in serious erosion-corrosion, which was consistent with the experiment results.

References

1. J. Mondal, K. Das and S. Das. *Wear*, 504-505 (2022) 204422.
2. R.S. Zheng, X.Y. Zhao, L.L. Dong, G. Liu, Y. Huang and Y.Z. Xu. *Eng. Fail. Anal.*, 138 (2022) 106333.
3. G. Schmitt and M. Bakalli. *Mater. Corros.*, 59 (2008) 181.
4. M. Abedini and H. M. Ghasemi. *Mater. Corros.*, 67 (2016) 513.
5. M. Kumar, H. Singh and N. Singh. *Mater. Corros.*, 66 (2015) 695.
6. J. Xu and C. Zhuo. *Mater. Corros.*, 61 (2010) 7.
7. W.Z. Wang, J.Y. Hu, X. Yuan, L. Zhou, J.S. Yu, Z. Zhang and X.K. Zhong. *Constr. Build. Mater.*, 342 (2022) 127972.
8. A. Rajput, J. Ramkumar and K. Mondal. *Wear*, 494-495 (2022) 204245.
9. H. Xu and A. Neville. *Mater. Corros.*, 53 (2022) 5.
10. B.Y. Hong, Y.B. Li, X.P. Li, G. Li, A.D. Huang, S.P. Ji, W.D. Li, J. Gong and J. Guo. *Petrol. Sci.*, 19 (2022) 1347.
11. R.B. Nair, H.S. Arora and H.S. Grewal. *Adv. Eng. Mater.*, 22 (2020) 2000626.
12. D.R. Qu, Y.G. Zheng, H.M. Jing, X. Jiang and W. Ke. *Mater. Corros.*, 56 (2005) 533.
13. H. Olia, M. Ghobadi, I. Danaee and S. Onsori. *Mater. Corros.*, 71 (2020) 1361.
14. C.C. Saenz-Betancourt, S.A. Rodríguez and J.J. Coronado. *Wear*, 498-499 (2022) 204330.
15. Z.L. Liu, A. Khan, M.L. Shen, S.L. Zhu, C.L. Zeng, F.H. Wang and C. Fu. *Tribol. Int.*, 173 (2022) 107618.
16. Ł. Szymański, E. Olejnik, J.J. Sobczak, M. Szala, P. Kurtyka, T. Tokarski and A. Janas. *J. Mater. Process. Tech.*, 308 (2022) 117688.
17. M.A. Islam, Z.N. Farhat, E.M. Ahmed, A.M. Alfantazi. *Wear*, 302 (2013) 1592.
18. Y.F. Tian, H.X. Li, S.P. Wang and Y.P. Fan. *Mater. Corros.*, 72 (2021) 1899.
19. C.M. Chun, N.V. Bangaru, N. Thirumalai, J.R. Peterson, C.J. Fowler and R.L. Antram. *Int. J. Appl. Ceram. Tec.*, 5 (2008) 597.
20. G. Yasin, M. Arif, M. Shakeel, Y.C. Dun, Y. Zuo, W.Q. Khan, Y.M. Tang, A. Khan and M. Nadeem. *Adv. Eng. Mater.*, 20 (2018) 1701166.
21. W.M. Chan, F.T. Cheng and W.K. Chow. *J. Am. Water Works Ass.*, 94 (2002) 76.
22. O. Joshua, R. Callum, B. Richard and A. Nevillea. *Wear*, 414-415 (2018) 376.
23. E. Raheem, E. Richard, O. Ikechukwuka, G. Kennell, R. Gerspacher and A. Odeshi. *Wear*, 410-411 (2018) 149.

24. B. Heider, M. Oechsner, T. Engler, J. Ellermeier, U. Reisgen, R. Sharma, E. Zokoll and E. Gonzalez. *Materialwiss. Werkst.*, 50 (2019) 1165.
25. S. Zhou, M.M. Stack and R.C. Newman. *Corrosion*, 52 (1996) 934.
26. K.S. Tan, J.A. Wharton, R.J.K. Wood. *Wear*, 258 (2005) 629.
27. X.L. Yang, J.L. Fei, S.H. Wang, Y. Gong and Z.G. Yang. *Mater. Corros.*, 70 (2019) 906.
28. R.K. Sharma, R.K. Das and S.R. Kumar. *Materialwiss. Werkst.*, 53 (2022) 675.
29. Y. Tian, H. Zhao, R. Yang, X. Liu, X. Chen, J. Qin, A. Mcdonald and H. Li. *Mater. Design*, 213 (2022) 110314.
30. P. Niederhofer, S. Siebert, S. Huth, W. Theisen and H. Berns. *Steel Res. Int.*, 86 (2015) 1439.
31. I.A. Maekai, G.A. Harmain, Zehab-ud-Din and J.H. Masoodi. *Int. J. Refract. Met. H.*, 105 (2022) 105830.
32. S.C. Cha and P. Wölpert. *Adv. Eng. Mater.*, 5 (2003) 213.
33. M.A. Chowdhury, N. Hossain, M. Shahin, U.K. Debnath, M. Rahman and M.M. Rahman. *Tribol. Int.*, 167 (2022) 107403.
34. H. Arabnejad, H. Uddin, K. Panda, S. Talya and S.A. Shirazi. *Powder Technol.*, 394 (2021) 1186.
35. E. Nakhostin, S. Kenny and S. Sivathayalan. *Eng. Struct.*, 260 (2022) 114217.
36. Z. Klenowicz, K. Darowicki, S. Krakowiak and A. Krakowiak. *Mater. Corros.*, 54 (2003) 181.
37. R.J. Chung, J. Jiang, C. Pang, B. Yu, R. Eadie and D.Y. Li. *Wear*, 477 (2021) 203771.
38. V.R. Kiragi, A. Patnaik and T. Singh. *Materialwiss. Werkst.*, 50 (2019) 1250.
39. V. Alar, I. Žmak, I. Stojanović, V. Šimunović and Z. Čeralinac. *Materialwiss. Werkst.*, 48 (2017) 785.
40. R. K. Sharma,R. K. Das,S. R. Kumar. *Materialwiss. Werkst.*, 52 (2021) 1173.
41. E. Chantziara, K. Lentzaris, A.G. Lekatou and A.E. Karantzalis. *Fatigue Fract. Eng. M.*, 42 (2019) 1548.
42. C.E. Fowler, J.E. Creeth, A.J. Paul, C. Carson, G. Tadesse and A. Brown. *Surf. Interface Anal.*, 53 (2021) 528.
43. Z.B. Zheng, J. Long, S. Wang, H. Li, J. Wang and K.H. Zheng. *Corros. Sci.*, 184 (2021) 109382.
44. G.Y. Gao and Z. Zhang. *Wear,* 488-489 (2022) 204137.
45. V. Javaheri, S. Sadeghpour, P. Karjalainen, M. Lindroos, O. Haiko, N. Sarmadi, S. Pallaspuro, K. Valtonen, F. Pahlevani, A. Laukkanen and J. Kömi. *Wear*, 496-497 (2022) 204301.
46. A.V. Krishnan and C.Y.H. Lim. *J. Mater. Res. Technol.*, 14 (2021) 1052.
47. L.M. Vilhena, C.M. Fernandes, J. Sacramento, A.M.R. Senos and A. Ramalho. *Lubr. Sci.*, 34 (2022) 247.
48. W.Z. Zhai, L.C. Bai, R.H. Zhou, X.L. Fan, G.Z. Kang, Y. Liu and K. Zhou. *Adv. Sci.*, 8 (2021) 2003739.
49. M.S. Khan and C. Sasikumar. *Eng. Fail. Anal.*, 139 (2022) 106491.
50. A. Rajput, J. Ramkumar and K. Mondal. *Ultrason. Sonochem.*, 71 (2021) 105399.
51. N. Kumar and N. Arora. *Mater. Lett.*, 284 (2021) 128932.
52. H.B. Wang, X.T. Liu, J.J. Che, H.W. Zhao, B. Bhushan, J. Tong, J. Zhuang and Y.H. Ma. *Materialwiss. Werkst.*, 51 (2020) 452.
53. M.H. Buszko, A.K. Krella, A. Marchewicz and G. Gajowiec. *Tribol. Int.*, 153 (2021) 106648.
54. G.D. Roque-Torres, S.R. Kwon, U. Oyoyo and Y.M. Li. *Microsc. Res. Techniq.*, 83 (2020) 1450.
55. S.R. Kumar, A. Patnaik and I.K. Bhat. *Materialwiss. Werkst.*, 51 (2020) 96.
56. A. Uzi and A. Levy. *Chem. Eng. Technol.*, 41 (2018) 1511.
57. H. Slot, D. Matthews, D. Schipper and E. van der Heide. *Fatigue Fract. Eng. M.*, 44 (2021) 199.
58. M.F. Mu, L. Feng, Q. Zhang, W.S. Zang and H.X. Wang. *Energy Sci. Eng.*, 10 (2022) 96.
59. J. Domitner, M. Aigner, T. Stern, A. Paar, C. Sommitsch and L. Elizondo. *Steel Res. Int.*, 91 (2022) 1900478.
60. R.F. Guo, P. Shen, N. Guo, L.K. Yang and Q.C. Jiang. *Adv. Eng. Mater.*, 20 (2018) 1800540.
61. P. Zhang, H. Qiu, L. Cao, X.H. Tu, J. Cui, H.L. Yu, J. Li, Q.W. Wang, J.J. Yang, W. Li and H.J.

Lin. *Tribol. Int.*, 175 (2022) 107866.
62. J.H. Liang, H.L. Gao, S.B. Xiang, L. Chen, Z.C. You and Y.C. Lei. *Wear*, 508-509 (2022) 204468.